Forward-calculated analytical interferograms in pass-through photon-based biomedical transillumination

Paulino Vacas-Jacques,* Marija Strojnik, and Gonzalo Paez

Centro de Investigaciones en Optica, Apartado Postal 1-948, 37000, Leon, Guanajuato, Mexico
*Corresponding author: pvj@cio.mx

Recently, we have introduced a transillumination technique for biomedical diagnosis. The technique, pass-through photon-based transillumination, relies on interferometric measurements to recover the information of interest. In this work, we present the forward-calculated analytical interferograms that describe the behavior of the system. Stochastic modeling of radiation interacting with tissue enables determination of amplitude and phase parameters, indispensable for computation of the interferograms. Sample variability is assessed by studying tissue phantoms similar to those used in the experimental verification of the technique and that are representative of (abnormal) dental tissues. For tissue characterization, perfect recovery of the integrated attenuation ensues by employing spatially compact radiation sources. For tissue imaging, spatially extended sources with broad bandwidth are superior due to the implicit longitudinal coherence filter. For both applications, sample variability issues may be neutralized by permitting spatial divergence of scattered photons. © 2009 Optical Society of America

OCIS codes: 170.1650, 170.6935, 170.3880, 170.3660.

1. INTRODUCTION

During the past decades, health care professionals have witnessed noteworthy improvements in diverse fields of medicine. Specifically with respect to dentistry, in the past thirty years various preventive procedures have served to reduce the occurrence of dental caries and tooth decay. However, several important topics still need to be addressed. These topics include: the identification of early lesions and those progressing actively, thorough descriptions of the natural history of caries, and the proposal of objective methods for diagnosis [1]. In addition, the scientific community in dentistry is promoting a paradigm shift. Surgical interventions are gradually being set aside, and a more medically based approach is being adopted [2]. Such preventive approach implies the need of early detection, imaging, and characterization of incipient and hidden carious lesions [3].

Early development of caries manifests only as a demineralization of dental tissues. Furthermore, such lesions are reversible provided clinical strategies are employed. Hence, the potential value of early lesion detection resides in the possibility of treating patients with nonsurgical methods, including remineralization. However, traditional diagnostic methods exhibit limitations when utilized for detection of incipient and hidden carious lesions [4]. Therefore, alternative solutions are required to enable preventive intervention.

Diverse methods for detecting early demineralization of dental tissues have been proposed in the past decade [5]. These include detection systems based on electrical current measurements [6,7], digital radiography [8,9], as well as ultrasound [10,11] and optical techniques. The latter include quantitative light-induced fluorescence [12,13], optical coherence tomography [14,15], near-infrared imaging [16,17], and fiber optic transillumination [18,19]. In our group, we have proposed a transillumination interferometric setup for analysis of biomedical samples, including dental tissues [20]. In contrast to the optical techniques described before, pass-through photon-based transillumination does not employ diffuse radiation. Instead, we utilize pass-through (i.e., ballistic) radiation as the information carrier for diagnosis [21–25].

Pass-through photon-based transillumination may be especially suited for the detection of incipient and hidden carious lesions, because sound enamel is seemingly transparent to near-infrared (NIR) radiation [26]. Demineralization of enamel, however, increases tissue attenuation significantly. Thus traversal of ballistic photons through potential carious lesions is inhibited. The probability of light absorption per unit length μ_a [mm^{-1}] for sound enamel in the NIR region is fairly small: $\mu_a < 0.1$ mm^{-1}. In addition, the probability of scattering μ_s [mm^{-1}] is also weak for NIR radiation. The value of μ_s is equal to 0.3 mm^{-1} at 1310 nm. In stark contrast, the attenuating characteristics of demineralized enamel may increase up to fifty-fold. The attenuation coefficient $\mu_t = \mu_a + \mu_s$ at the same NIR wavelength is ≈ 18 mm^{-1} [27].

Penetration depth in a turbid medium such as enamel follows an exponential distribution. The expected value is given by the inverse of the attenuation coefficient of the medium. Thus, mean penetration depths at 1310 nm for sound and carious enamel can be 2.5 mm and 0.056 mm, respectively. Correspondingly, the probabilities of ballistic transmission through a 10 mm sample are 0.0183 and 0.

Hence, isolated detection of ballistic photons may provide a way of distinguishing between sound and carious enamel. Furthermore, pass-through photon-based techniques are appealing because of the sensitivity of the method in detecting changes in composition and morphology.

We are interested in describing the response of the transillumination technique for two applications: characterization and imaging. The former is aimed at providing quantitative description of the medium. Such information may enable objective assessment of samples, including incipient and hidden carious lesions. Meanwhile, the latter application may become the basis for an imaging modality similar to computed axial tomography. This approach, in turn, may complement the techniques being currently utilized to identify the presence of caries earlier.

In Section 2, we describe the importance of stochastic modeling and the procedure for recovering the optical properties of the sample in the transillumination interferometer. Dental tissue models, and their corresponding random walk attenuation coefficients, are addressed in Section 3. Section 4 is devoted to the calculation of the analytical response of the system, including the recovery of attenuation coefficients. In Section 5, we discuss system performance and 2-D imaging. Finally, we summarize the results of this work and present plausible future directions in pass-through photon-based biomedical transillumination.

2. THEORY

A. Mathematical Model
The mathematical model describing our experiment is rooted in partial coherence theory and has been discussed in detail [20]. In our proposal for biomedical diagnosis, the sample under test is located in one arm of an interferometer. The other arm includes a phase delay line. The electric field of the source is divided into reference $\mathbf{E}_r$ and sample $\mathbf{E}_s$ beams. The latter, in turn, is composed of forward-scattered $\mathbf{E}_{sc}$ and pass-through $\mathbf{E}_p$ contributions. At the detection plane, sample and reference fields are superposed and interference is observed:

$$P(t,T_{sc}) \propto \langle \{[\mathbf{E}_r(\tau+t) + [\mathbf{E}_p(\tau) + \mathbf{E}_{sc}(\tau+T_{sc})]\}$$
$$\times \{\mathbf{E}_r(\tau+t) + [\mathbf{E}_p(\tau) + \mathbf{E}_{sc}(\tau+T_{sc})]\}^*\rangle. \quad (1)$$

Here, P stands for detected power, τ is the reference time for partial coherence modeling, t represents the modulation time, and T_{sc} describes the random time that scattered photons take to traverse the sample. The chevrons denote time average and the asterisk demarcates complex conjugation. Throughout this work, we use bold letters for complex-valued quantities.

By relating reference and sample beams to the incident field of the source, we arrive at the partial coherence model describing the experiment:

$$P(t,T_{sc}) = \Gamma_{i,i}(0)((1-k_{sp1})(1-k_{sp2}) + k_{sp1}k_{sp2}|\boldsymbol{\gamma}_m|^2$$
$$+ k_{sp1}k_{sp2}|\boldsymbol{\gamma}_{sc}|^2 + 2k_{sp1}k_{sp2}|\boldsymbol{\gamma}_m||\boldsymbol{\gamma}_{sc}|$$
$$\times |\boldsymbol{\gamma}_{i,i}(T_{sc})|\cos[\Phi_{i,i}(T_{sc})]$$
$$+ 2\sqrt{k_{sp1}}\sqrt{1-k_{sp1}}\sqrt{k_{sp2}}\sqrt{1-k_{sp2}}$$
$$\times \{|\boldsymbol{\gamma}_m||\boldsymbol{\gamma}_{i,i}(t)|\cos[\Phi_{i,i}(t)] + |\boldsymbol{\gamma}_{sc}||\boldsymbol{\gamma}_{i,i}(t+T_{sc})|$$
$$\times \cos[\Phi_{i,i}(t+T_{sc})]\}). \quad (2)$$

Here, $\Gamma_{i,i}(0)$ is the total collected power upon proving a small area. k_{sp1} and k_{sp2} denote the splitting coefficients of the beam dividers. $|\boldsymbol{\gamma}_{i,i}(\tau)|$ and $\Phi_{i,i}(\tau)$ designate amplitude and phase of the complex degree of self-coherence. In addition, $\boldsymbol{\gamma}_m$ and $\boldsymbol{\gamma}_{sc}$ are the complex material and scattering coherence functions. The former describes the ballistic exponential attenuation of the incident field, the latter relates forward-scattered to incident fields.

The expression in Eq. (2) is most useful in understanding the recovery of information from interferometric quantities. An alternative interpretation of the transillumination technique follows from the theory of low-coherence optical tomography [28]. Such interpretation provides additional benefits. First, a distinctive feature of the transillumination interferometer is highlighted. Second, the interpretation contextualizes the proposal within the scope of other well-established biomedical techniques. Third, it provides a seemingly intuitive approach for calculating the analytical response of the interferometer. For these reasons, we assess the transillumination interferometer in the context of the theory of low-coherence optical tomography.

In analogy to Eq. (1), the detected power is found by superposition of sample and reference beams:

$$P(\Delta L/c) = \left\langle \left[\int_{-\infty}^{\infty} \mathbf{E}'_s(\tau,L_s)\mathrm{d}L_s + \mathbf{E}_r(\tau+t) \right] \right.$$
$$\left. \times \left[\int_{-\infty}^{\infty} \mathbf{E}'_s(\tau,L_s)\mathrm{d}L_s + \mathbf{E}_r(\tau+t) \right]^* \right\rangle. \quad (3)$$

Here, $\Delta L = L_r - L_s$ is the optical path-length difference between interfering beams, c stands for light velocity in vacuum, L_r and L_s are optical path-lengths of reference and sample arms, and $\mathbf{E}'(\tau,L_s)$ is defined as the path-length-resolved field density, $\mathbf{E}'(\tau,L_s) = \partial\mathbf{E}(\tau,L_s)/\partial L_s$.

Equation (3) represents the multiple interactions between sample and reference beams. Sample path-lengths are independent of the reference scan delay. Therefore, we may rewrite Eq. (3) as

$$P(L_r) = P_r + P_s + 2(P_rP_s)^{1/2}$$
$$\times \int_{-\infty}^{\infty} [T(L_s)]^{1/2}|\boldsymbol{\gamma}_{i,i}(\Delta L)|\cos[\Phi_{i,i}(\Delta L)]\mathrm{d}L_s, \quad (4)$$

where

$$P_r = \langle \mathbf{E}_r(\tau+t)\mathbf{E}_r^*(\tau+t)\rangle,$$

$$P_s = \left\langle \int_{-\infty}^{\infty} \mathbf{E}_s'(\tau,L_s)\mathrm{d}L_s \int_{-\infty}^{\infty} \mathbf{E}_s'^*(\tau,L_s)\mathrm{d}L_s \right\rangle,$$

$$T(L_s) = [\mathrm{d}P_s(L_s)/\mathrm{d}L_s]/P_s.$$

P_r and P_s are the dc contributions of the reference and sample fields. In addition, $T(L_s)$ is the path-length-resolved transmittance. In reflection geometries, $T(L_s)$ is replaced by the path-length-resolved reflectance.

The offset in Eq. (4) does not contribute to the signal because it is filtered. Thus, the interferometer response is described by the convolution

$$P(L_r) = 2(P_r P_s)^{1/2}([T(L_s)]^{1/2} \otimes \{|\boldsymbol{\gamma}_{i,i}(L_s)|\cos[\Phi_{i,i}(L_s)]\}).$$
(5)

Here $\otimes$ denotes the convolution operator. From the convolution theorem, the preceding equation may be calculated by passing the path-length-resolved transmittance through a filter. The shape of the filter is determined by the power spectrum of the source. The central frequency of emission determines the localization of the filter. Meanwhile, the emission bandwidth establishes the extent of filtering. For radiation sources employed in partial-coherence interferometry, filters have narrow bandwidths and are centered at high frequencies. Thus, the system is mainly sensitive to the fast-varying components of $[T(L_s)]^{1/2}$.

It is precisely this feature that is most suitable for pass-through transillumination. Ballistic radiation represents an ideal high-frequency component of sample transmittance. Therefore, the transillumination interferometer is highly sensitive to the information of interest. This is a salient characteristic of our proposal. As sample attenuation increases, the behavior of the system resembles more that of traditional low-coherence optical tomography. Eventually, when solely diffuse radiation emerges from the sample, both systems are comparable.

Equations (2) and (4) are equivalent descriptions of the transillumination interferometer. However, the latter provides a more intuitive approach for calculating the analytical response of the interferometer. In essence, we compute the convolution of the self-coherence function with $[T(L_s)]^{1/2}$. The former is a feature of the instrument, whereas the latter is characteristic of the sample. To determine amplitude and phase parameters of the interferograms, we resort to stochastic modeling for describing the interactions between radiation and turbid media.

B. Stochastic Analysis
The assessment of the partial-coherence interferometer would be straightforward if the sample under test were purely transparent. The scenario is rather different when the evaluation of a turbid sample is in order. Photon transport in turbid media is modeled as a random walk process in three dimensions [29,30]. Thus, the description of radiation–tissue interactions is not deterministic, but rather stochastic. In addition, a comprehensive account of the random process is required for the evaluation of the

interferometer. Thus, we have written a Monte Carlo (MC) code to determine the outcome of the stochastic process as needed for our application.

In MC simulations, a specific amount of radiation is subdivided into a number of packets of photons. Each of these individual packets, or ensembles, is then propagated through the sample. The position for starting the propagation of an ensemble is determined randomly, by sampling the spatial distribution of the source. Flat-field, Gaussian, and point-source distributions may be selected in our code. The initial direction of propagation of the packet is identical to that of the beam, and need not be collinear with the optical axis.

The ensemble propagates deterministically in transparent media, such as glass or air. In random media, however, the description of radiation transport accords with the Markov property of stochastic processes. Thus, the packet of photons takes random steps and may scatter regardless of prior history. The step size or penetration depth of the ensemble is computed by sampling an exponential distribution. Path-length information ensues from these random and deterministic steps. In the program, we store this information as time-of-flight values [25]. When the packet of photons traverses the medium in one step, it is classified as ballistic. In any other case, part of the ensemble is absorbed, and its weight is reduced accordingly. If the packet of photons is still significant, it proceeds to vary randomly its propagation direction.

The directional dependence of scattering in the medium is described by a phase function [31,32]. In the code, several phase functions related to dental enamel are available. These include the familiar Henyey–Greenstein and isotropic phase functions [32]. In addition, a modified Henyey–Greenstein phase function may be employed. This function describes more closely scattering in enamel tissues [27]. The new propagation direction of the ensemble is determined by sampling the corresponding phase function of the medium. Thereafter, the packet of photons propagates farther, until it is entirely attenuated or leaves the sample. Scattered packets of photons that are transmitted through the medium conform the diffuse transmittance. In addition, all packets of photons retain recollection of their three-dimensional journey, thus enabling the assessment of the transillumination interferometer.

The program described does not take into consideration depolarization effects or losses of spatial coherence. The former phenomenon may be incorporated in the analysis by representing the polarization in terms of the Stokes vector [33,34]. Meanwhile for coherent phenomena, an electrical field MC approach may be employed [35]. These two issues are of secondary importance for pass-through photons. Nevertheless, they do affect diffuse radiation. In this respect, our MC analysis represents a worst-case scenario for the transillumination interferometer. In addition, we should point out that conventional MC simulations yield the average diffuse reflectance (i.e., transmittance) of turbid media [36]. Therefore, the effects of multiply scattered radiation are somewhat underestimated. In our analysis, however, diffuse radiation represents optical noise, and an average measure of such behavior is adequate.

The path-length-resolved transmittance of pass-through photons exhibits a delta-like behavior. In our program, we trace each packet of photons individually. Therefore, whenever a packet of photons encounters an interface, transmitted and reflected packets are created. Thus, various delta-like peaks may appear as a result of Fresnel reflections. The path-length-resolved diffuse transmittance is calculated similarly to the reflected counterpart in low-coherence tomography. The single difference is that, after MC simulations, we fit the diffuse transmittance. The fitting function is a spline, which helps account for any discrete features in the data.

We conclude this section by describing the steps needed to compute the analytical response of the system. First, we perform the random walk simulations to determine path-length-resolved transmittances. Then, we calculate the convolution of Eq. (5) by making use of the convolution theorem. This approach helps lessen the computational burden. Finally, we note that only those photons inside the interference area are considered during calculations.

C. Recovery of Information
Pass-through photons provide a predictable measure of the integrated attenuation of the sample. In contrast, the information of forward-scattered photons is random. Moreover the expressions of interference, Eqs. (2) and (4), predict presence of signal comingled with noise. Therefore, isolation of the detected signal is necessary for accurate recovery of information. Hereafter we refer only to Eq. (2), because more insight is gained from this expression. After removing the fluctuating offset, the system response is composed exclusively of temporally modulated signals:

$$P(\vec{r},t,T_{sc}) = \Gamma_{i,i}(0)(2\sqrt{k_{sp1}}\sqrt{1-k_{sp1}}\sqrt{k_{sp2}}\sqrt{1-k_{sp2}}$$
$$\times\{|\boldsymbol{\gamma}_m(\vec{r})||\boldsymbol{\gamma}_{i,i}(\vec{r},t)|\cos[\Phi_{i,i}(\vec{r},t)]$$
$$+|\boldsymbol{\gamma}_{sc}(\vec{r},T_{sc})||\boldsymbol{\gamma}_{i,i}(\vec{r},t+T_{sc})|\cos[\Phi_{i,i}(\vec{r},t+T_{sc})]\}).$$
$$(6)$$

In contrast to Eq. (2), the expression without fluctuating offset includes the spatial dependence $\vec{r}$ explicitly. The undesired contributions of forward scattering may induce random variations. This hindrance may be overcome by employing a compact spatial extent or coherence filtering. Assuming that either procedure is successfully implemented, the temporal maximum of the detected power yields a proportional measure of the information of interest:

$$\max\{P(\vec{r},t)\} = 2\Gamma_{i,i}(0)\sqrt{k_{sp1}}\sqrt{1-k_{sp1}}\sqrt{k_{sp2}}\sqrt{1-k_{sp2}}$$
$$\times\mathcal{R}_g\prod_i \exp\left\{-\frac{1}{2}[\mu_{a_i}(\vec{r})+\mu_{s_i}(\vec{r})]D_i(\vec{r})\right\}.$$
$$(7)$$

Here, we have considered a radiation source with even power spectrum. Also, we have substituted the material coherence function [20]. $\mathcal{R}_g$ and $D_i(\vec{r})$ are the Fresnel reflection coefficient and the ith sample thickness. To recover the information of interest, we must cancel instrument-related contributions. For this purpose, a reference value of dc-filtered power P_{ref} is necessary. The resulting expression, after normalization, is

$$\mathcal{R}_g \exp\left\{\sum_i -\frac{1}{2}[\mu_{a_i}(\vec{r})+\mu_{s_i}(\vec{r})]D_i(\vec{r})\right\}$$
$$= \max\{P(\vec{r},t)\}/\max\{P_{ref}(\vec{r},t)\}. \quad (8)$$

In summary, for *in vitro* studies, we may recover the attenuation coefficient of the sample from interferometric quantities. This assertion is true whenever a sample of one constituent is assessed. For general *in vitro* or *in vivo* studies, the transillumination interferometer yields information similar to that of computed axial tomography (i.e., integrated values of attenuation).

3. DENTAL MODELS AND RANDOM WALK ATTENUATION COEFFICIENTS

A. Tissue Characteristics and Sample Variability
Accurate descriptions of the optical properties of turbid media are challenging. Absorption and scattering coefficients are required to emulate photon transport in turbid media. In addition, the scattering phase function is needed to determine the random propagation direction. In radiation–tissue interactions, scattering is predominantly forward directed [31,32]. Thus, polar-scattering and incident angles are similar to each other. In light propagation studies, this correspondence is expressed in terms of the anisotropy factor g, or expected value of the cosine of the polar angle.

In the ballistic interferometer, presence of optical noise is a function of scattering coefficient and anisotropy factor. Concerning enamel tissues, differences exist with respect to both parameters. On the one hand, reported scattering coefficients vary, e.g., from 1.5 mm^{-1} [37] to 5 mm^{-1} [38] at 700 nm. On the other hand, discrepancies are found in the anisotropy factor. The values range from 0.68 [37] to 0.96 [38]. These variations may result from differences in the design phase of the experiments. However, they could also be attributed to sample variability. Such variability represents a caveat for pass-through photon-based transillumination. Isolation of optical noise is more intricate when these parameters increase.

Lipid-based phantoms are not an exception with regard to differences in the optical properties between batches and trademarks. The most cited lipid-based material utilized as tissue phantom is Intralipid [39]. Diverse groups have studied the spectral optical properties of Intralipid for light propagation purposes. Specifically, van Staveren *et al.* [40] and Flock *et al.* [41] have made available least-square fits relating the optical properties of Intralipid 10% to wavelength. In this work, we utilize both references to construct three tissue models. The lipid-to-total-volume concentration considered is $6.25/1000\,[\mu l/\mu l]$. At this concentration, we have observed disparities between theory and experiment [20]. We are, therefore, interested in understanding more in detail the source of these deviations. In addition, the concentration is kept constant to emulate the certain variability between samples.
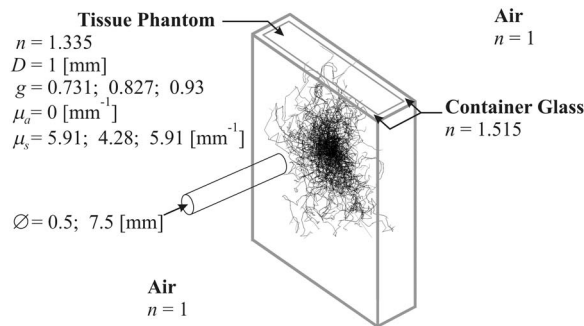
Fig. 1. Tissue models utilized in the random walk program are representative of abnormal dental samples. Semicolons separate the characteristics of each model.

Table 1. Summary of Tissue Models

Tissue Model	Reference	μ_a [mm^{-1}]	μ_s [mm^{-1}]	g^a
(1)	van Staveren *et al.* [40]	0	5.91	0.731
(2)	Flock *et al.* [41]	0	4.28	0.827
(3)	van Staveren *et al.* [40] and Flock *et al.* [41]	0	5.91	0.93

^{a}The Henyey–Greenstein phase function is employed in all calculations.

For the first two models, we use the aforementioned concentration and the data of van Staveren *et al.* and Flock *et al.* In the third model, we combine the information from both references. We utilize the scattering coefficient of van Staveren *et al.* [40]. In turn, the anisotropy factor is the weighted mean plus one standard deviation reported by Flock *et al.* [41]. Greater attenuation values and highly forward-directed scattering are distinctive features of most biological tissues. The resulting tissue models are shown in Fig. 1 and summarized in Table 1.

In Fig. 1, we separate by semicolons the optical properties of the three scenarios. In all cases, the sample is contained in a 1 mm thick cuvette surrounded by air. Moreover, the radiation impinging on the sample is visible. The attenuation of the lipid phantom in the red portion of the spectrum is comparable to that of enamel in the NIR. More specifically, the attenuation of the dental models is representative of abnormal enamel. Values of optical depth are greater than those expected for sound enamel. Finally, two beam sizes are also shown. These represent

the applications of characterization, $\varnothing = 0.5$ mm, and imaging, $\varnothing = 7.5$ mm.

B. Random Walk Attenuation Coefficients
Previously, we have evaluated the number of particles that need to be assessed in the stochastic computations [25]. We found that the use of 100,000 photons yields statistically significant results for the study of enamel tissues. The standard deviation of total transmittance was shown to be zero up to the third decimal place. This is most important for the calculation of reference attenuation coefficients, because a determined "random walk" uncertainty exists. Considering the attenuation of the media discussed in this work, the "random walk" uncertainty is more considerable for the first and third tissue models. However, Monte Carlo simulations are known to be time-consuming. Thus, we employ the same number of photons in all computations.

We perform two random walk simulations—for characterization and imaging—of each dental model. Following the stochastic analyses, we determine random walk uncertainties and attenuation coefficients. For this purpose, ballistic transmittance values are necessary. We divide into ten subsets the total amount of assessed particles. We then calculate mean, standard error of the mean, and 99% confidence intervals (CI) of ballistic transmittance. It is the standard error of the mean that we define as the random walk uncertainty.

Attenuation coefficients are related to transmittance values through an exponential function. In addition, the determination of attenuation coefficients requires the cancellation of Fresnel reflections. All information needed is available from the random walk program. We employ it to calculate expected values and 99% CI of the attenuation coefficients. In Table 2, we present the statistical findings for the stochastic processes under study.

The attenuation coefficients input to the stochastic program are listed in Table 1. Meanwhile, those resulting from the random simulations are described in Table 2. A comparison between these values serves to establish that the former are subsumed in the 99% CI of the latter. Furthermore, from the data of Table 2, we ascertain that the random walk uncertainty is more considerable for the first and third tissue models. Nonetheless, attenuation coefficient variability remains in the first decimal digit. In

Table 2. Pass-Through Transmittance Values and Reference Random Walk Attenuation Coefficients

Tissue Model	Intended Application	Pass-Through Transmittance^a	99% Confidence Intervals	Attenuation Coefficient [mm^{-1}]	99% Confidence Intervals^b [mm^{-1}]
(1)	Characterization	0.00276 ± 0.00017	[0.00232, 0.00320]	5.799	[5.652, 5.972]
(2)	Characterization	0.01238 ± 0.00036	[0.01145, 0.01330]	4.298	[4.226, 4.376]
(3)	Characterization	0.00260 ± 0.00014	[0.00224, 0.00297]	5.857	[5.726, 6.007]
(1)	Imaging	0.00242 ± 0.00018	[0.00196, 0.00288]	5.929	[5.755, 6.141]
(2)	Imaging	0.01322 ± 0.00030	[0.01246, 0.01399]	4.232	[4.176, 4.292]
(3)	Imaging	0.00229 ± 0.00014	[0.00194, 0.00265]	5.983	[5.841, 6.150]

^{a}The first value corresponds to the sample mean, the second to the standard error of the mean. For the standard error of the mean, we estimate the standard deviation by calculating the square root of the sample variance.

^{b}Confidence intervals for the attenuation coefficients are determined from the corresponding values for pass-through transmittances.

what follows, the benchmark coefficients are the mean values listed in Table 2 instead of the quantities input to the random walk program.

4. ANALYTICAL INTERFEROGRAMS AND RECOVERED ATTENUATION COEFFICIENTS

In order to calculate the response of the system, certain parameters of partial-coherence interferometry are needed. We begin by describing the spatial characteristics of the source. The transversal distribution of the collimated beam is flat-field. The spatial extent is 0.5 mm for characterization and 7.5 mm for imaging (refer to Fig. 1). Each value determines the area for collecting transmitted photons after random walk computations.

The spectral signature of the source determines the longitudinal coherence filter. We evaluate two partially coherent sources with Gaussian spectra. The first exhibits a narrow emission, while the second has a broader bandwidth. The former is representative of a commercially available superluminescent diode. The center wavelength $\bar{\lambda}$ is 640 nm, while the bandwidth $\Delta\lambda$ equals 8 nm. The latter source emulates the light emitting diode employed during the experimental verification of the technique ($\bar{\lambda} = 637$ nm and $\Delta\lambda = 20$ nm). Finally, the detection plane is located 1 mm after the sample. Path-length-resolved transmittances and forward-calculated interferograms are depicted in Fig. 2.

The results are arranged as follows. The sample under consideration is identified by the model number, which is placed on the upper left corner of each representation. In the upper part of the path-length-resolved transmittance plot, we distinguish between applications. To construct the abscissa of these representations, we subtract the least path-length traversed by transmitted photons. The ordinate is divided into two parts. Such feature allows the details of both ballistic and diffuse contributions to be observed. Moreover, in the inset, we depict the analytical interferograms for narrow (top) and broad (bottom) emission sources. The x axes of the interferograms span four coherence lengths and may be used to differentiate narrow from broad radiation sources.

Sample variability is clearly an important issue to consider in the interferometer. Detection of optical noise is closely related to the optical properties of the sample. In general, for tissue characterization purposes, a compact spatial extent is desirable. Nonetheless highly forward-directed scattering is difficult to overcome, even when the size of the source is compact. This assertion is verified by analyzing the path-length-resolved transmittances. Specifically, the contributions of diffuse radiation increase approximately fivefold. This occurs when the anisotropy factor varies from 0.731, model (1), to 0.93, model (3).

The behavior of the partial coherence interferometer as a narrow band-pass filter, centered at high frequencies, is manifest in the interferograms. The transillumination technique is highly sensitive to the information of interest. Thus, both radiation sources perform alike. However, a portion of diffuse radiation is quasi indistinguishable from the ballistic. Masking of ballistic photons is more im-

portant when attenuation increases. This assertion may be validated by comparing the proportion of ballistic to diffuse contributions from models (2) and (3).

For imaging applications, we are interested in obtaining 2-D representations. Therefore, as a preliminary for imagery of tissues, we assess the response when increasing significantly the spatial extent. As expected, tissue imaging plots in Fig. 2 exhibit more intermingled presence of forward-scattered and pass-through photons. Similarly to the case of tissue characterization, variability in the optical properties is important. Different samples behave distinctly depending on their scattering characteristics. Furthermore, the effects of highly forward-directed scattering and marked attenuation are similar to those described for tissue characterization. However, masking of ballistic photons by diffuse radiation is more easily identified. This assertion may be verified by analyzing the second etalonlike reflection of ballistic radiation.

For imaging purposes consisting of spatially extended sources, the utilization of broadband radiation is desirable. This stems from the implicit longitudinal coherence filter of the source. However, the transillumination interferometer is rather flexible in terms of the broadness of emission. The latter assertion is valid when diffuse photons do not obscure the ballistic counterpart. Such behavior may be corroborated from the interferograms.

Multiple interactions between radiation and tissue change the propagation direction of diffuse radiation. Most probably, diffuse photons will diverge gradually after leaving the sample. We make use of this fact before dealing with the recovery of information. Emphasis is placed on proposing complementary methods to effectively isolate the signal of interest, thus providing a solution to counteract sample variability issues. In Fig. 3, we present the results when the interference plane is located 200 mm away from its previous position.

Qualitative improvements in system response are easily seen in Fig. 3. There are fewer—or even an absence of—diffuse contributions in path-length-resolved transmittances. This behavior implies efficient filtering of optical noise. Nonetheless, imaging applications tend to exhibit the presence of diffuse radiation. Highly forward-scattering remains the principal source of noise. However, the interferometer response is governed mainly by the signature of ballistic radiation.

The recovery of attenuation coefficients from interferometric quantities is seemingly straightforward. As illustrated in Eq. (8), maxima of dc-filtered sample and reference interferograms determine the sought information. The data of the sample interferograms are available from Figs. 2 and 3. However, reference data needs be determined. For this purpose we assess anew the model of Fig. 1 with the scattering coefficient set to zero. The corresponding value of maximum dc-filtered power reads 0.17041. Reference calculations serve to account for Fresnel reflections. In addition, sample thickness is 1 mm. Thus, twice the logarithm of maxima ratios yields the information sought. In Table 3, we list the recovered coefficients.

As expected, we ascertain that recovered attenuation coefficients exhibit discrepancies. These are due to the influence of optical noise. The presence of such differences
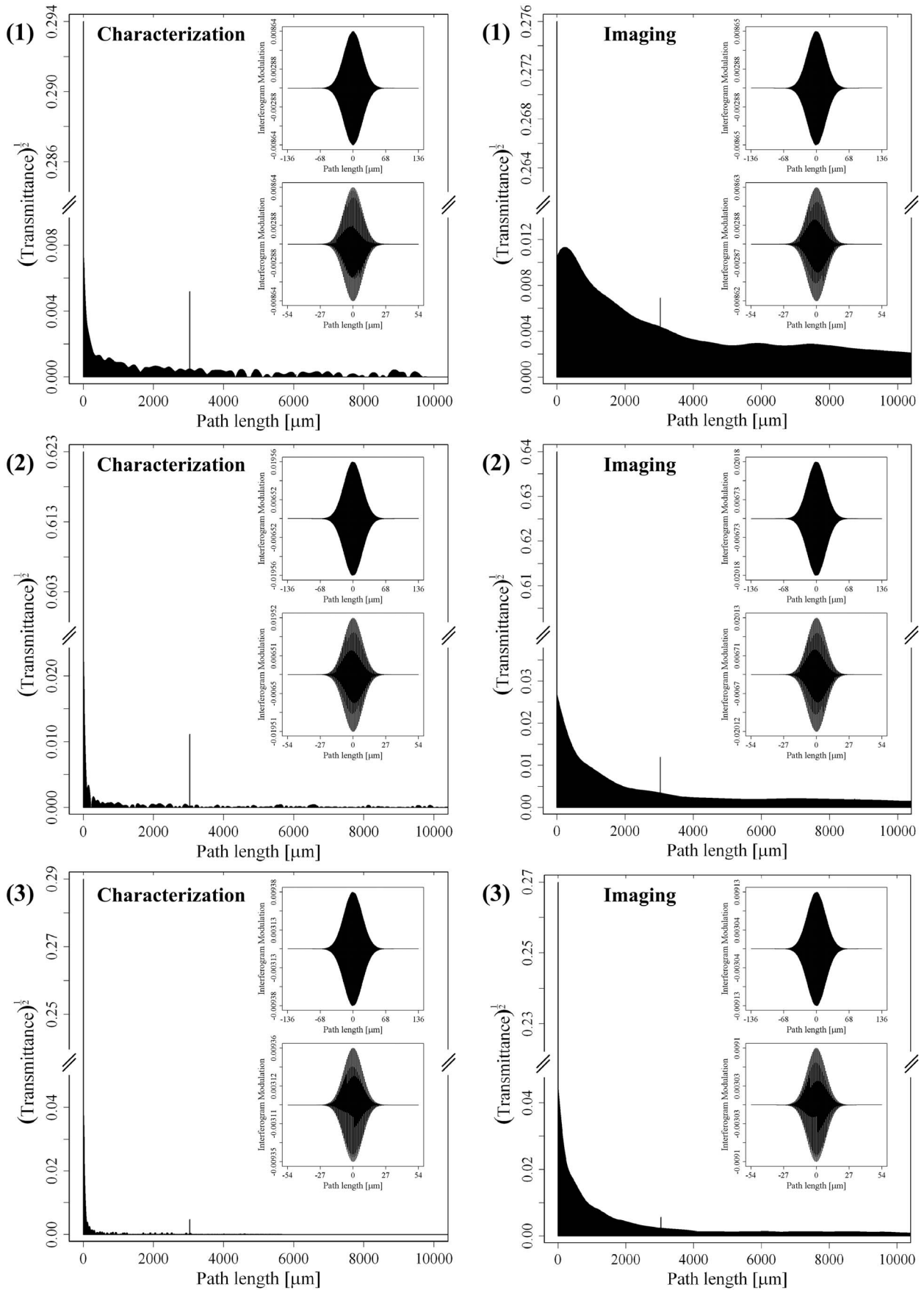
Fig. 2.   Path-length-resolved transmittances exhibit sample variability effects for characterization and imaging. Analytical interferograms for narrow and broad bandwidths are shown in each inset. The numbers in the upper left corner refer to the model under study.
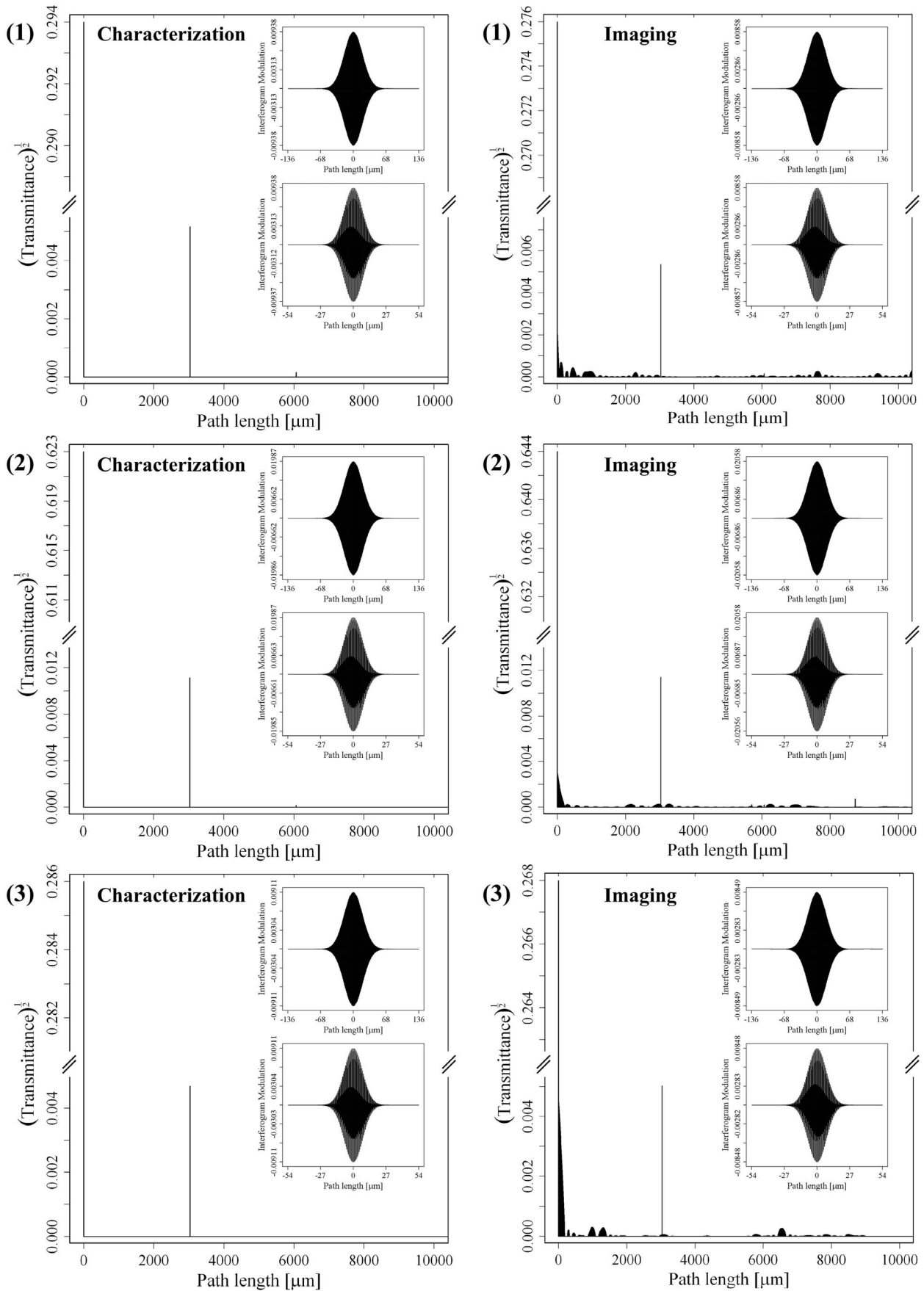
Fig. 3. The superposition plane is displaced to minimize the presence of diffuse radiation. Qualitative improvements in system response are easily seen.

Table 3. Attenuation Coefficients [mm^{-1}]^a Recovered from Interferometric Quantities

Characterization						Imaging					
Model (1)		Model (2)		Model (3)		Model (1)		Model (2)		Model (3)	
Near	Far	Near	Far	Near	Far	Near	Far	Near	Far	Near	Far
5.964	5.799	4.330	4.298	5.800	5.857	5.962	5.978	4.267	4.228	5.854	5.999
5.963	5.799	4.334	4.298	5.804	5.857	5.966	5.977	4.272	4.228	5.860	6.000
5.799		4.298		5.857		5.929		4.232		5.983	

^{a}The first two rows of attenuation coefficients correspond to those of narrow and broad emission sources, in that order. The last row shows the reference attenuation coefficients of Table 2. Column headers 'Near' and 'Far' refer to the position of the detection plane; the associated coefficients pertain to the data of Figs. 2 and 3, respectively.

is a function of the variability between samples. Nonetheless, the overall behavior of the interferometer was shown to be enhanced by permitting spatial divergence of unwanted radiation. This behavior, which implies neutralization of sample variability, is also corroborated by analyzing the recovered coefficients. In fact, perfect recovery is exhibited for spatially compact sources. Nevertheless, ideal collimation is far from being trivial for such small sizes. Collimation issues are secondary for greater spatial extents. However optical noise is more liable to be encountered because of the increase in area dimensions. The effects of coherence filtering are positive in these cases. Broader bandwidths are, therefore, recommended for tissue imaging applications.

5. DISCUSSION

In addition to the effects of forward-scattered radiation, other factors may influence the recovery of integrated attenuation. First, we should consider whether adequate offset filtering is important. The dc term is not only deterministic, but it is also composed of random contributions. Another factor that is equally important is the accurate determination of maximum power. Precise maxima values become more difficult as attenuation increases, because fewer ballistic photons traverse the medium. However, since relative values are in play, peak and offset varia-

tions induce similar inaccuracies. Hence, we concentrate exclusively on those pertaining to power.

Let P_ϵ and ϵ denote percentage deviation of power and error in the recovered integrated attenuation, respectively. Then, by making use of the multiplication identity of logarithms and Eq. (8), we find $\epsilon = \pm 2 \ln(P_\epsilon)$. Especially if the detected signal is feeble, errors in recovered integrated attenuation may be significant. Such deviations may account for the disparities observed in previous experiments [20], and may emerge from at least two scenarios. First, when the radiation source is not capable of providing sufficient power. Second, when detection electronics are not sensitive enough. Thus, as a result of this work, we are currently assessing possible improvements to the transillumination setup. These include improvements of the detection scheme, or the implementation of an autocorrelation interferometer [42].

We have emphasized that compact spatial extent enables characterization of selected turbid media. Specifically, the samples we have discussed are equivalent to dental enamel. Thus, pass-through photon-based transillumination may be favorable for characterization of early dental decay. This approach could yield an objective method for diagnosis of incipient and hidden caries. However, 2-D representations are also required to complement the techniques being currently utilized to identify the presence of caries earlier. Precisely for this reason, we
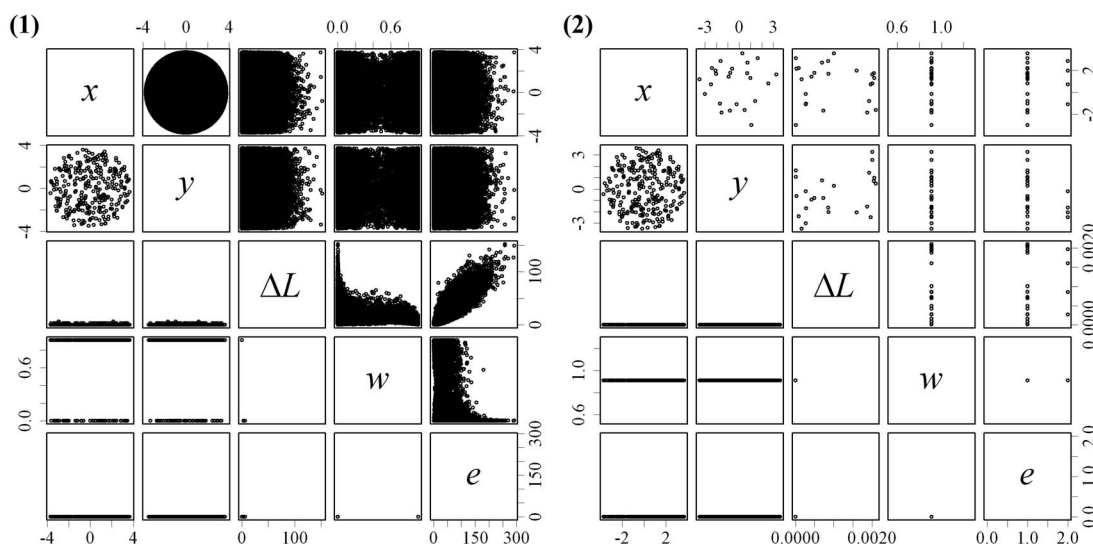

Fig. 4.   Pass-through and forward-scattered contributions are comingled in 2-D scenarios. Emission bandwidths narrow (1) and broad (2) determine filtering efficacy.

have suggested the use of a spatially extended broadband source. Such source enables 2-D analyses and optical filtering simultaneously. The proposal is rather straightforward, and the theoretical bases have been explored in this work. The main difference, for tissue imaging applications, is the need for 2-D detection schemes.

As a qualitative prelude for tissue imaging, we illustrate the effects of coherence filtering in 2-D applications. In Fig. 4, we present scatter plots of multivariate data from one of the random processes. We utilize the first tissue imaging model as the sample. We depict unique photons with path differences of at most one coherence length, and detection occurs immediately after leaving the medium.

In Fig. 4, we assess the behavior of narrow and broad bandwidth sources. The response of the former, a He–Ne laser ($\bar{\lambda}=632.8$ nm and $\Delta\lambda=0.001$ nm), is numbered (1). The behavior of the latter, a broadband source ($\bar{\lambda}=637$ nm and $\Delta\lambda=200$ nm), is labeled (2). In each representation, x and y are Cartesian position coordinates. ΔL is path-length difference. w represents the weight of each particle, and e corresponds to the number of scattering events. The first three variables are expressed in millimeters, whereas the last two are dimensionless. Reading of these plots, computed in R [43], is simple. Each row–column intersection represents a scatter plot of the corresponding variables in the diagonal. Data below and above the diagonal correspond to that of pass-through and forward-scattered photons, respectively.

Coherence filtering effects are evident in Fig. 4. The narrow emission source does not provide a mechanism to isolate signal from noise. In contrast, the improvement is noteworthy with a broadband source. Thus, broadband transillumination may be especially suited to determine maps of integrated attenuation (i.e., to identify the presence of caries earlier).

6. SUMMARY AND FUTURE WORK

We have presented the methodology to forward-calculate the interferograms describing pass-through photon-based biomedical transillumination. The interferograms may be determined by convolving the path-length-resolved transmittance with the self-coherence of the source. The transillumination interferometer was shown to be highly sensitive to the information of interest. Ballistic radiation is an ideal high-frequency component of sample transmittance. Furthermore, we have proposed a method to recover the integrated attenuation from interferometric quantities. Maxima of normalized dc-filtered power are required for this purpose.

The feasibility of implementing the technique to detect incipient and hidden caries was discussed. Three tissue models mimicking the attenuation of abnormal enamel were proposed. These served to assess sample variability. We performed two random walk computations—for characterization and imaging—of each dental model. From the stochastic analyses, we calculated statistical measures and 99% CI for ballistic transmittance. Furthermore, these values were the bases to compute reference random walk attenuation coefficients. We then calculated

the analytical interferograms and compared the recovered attenuation coefficients.

For tissue characterization purposes, perfect recovery of the integrated attenuation resulted from use of spatially compact sources. For imaging of tissues we established that spatially extended sources with broad bandwidths are superior. In both applications, variability in the optical properties of the samples was shown to induce different degrees of noise. Spatial divergence of scattered photons was suggested to neutralize sample variability. In addition, we discussed the influence of inaccuracies in offset and maxima values. Sample variability and instrumentation features must be considered during the implementation of the technique.

Our future work will focus on the construction of a system to assess dental samples. However, we must first consider the spectral dependence of the transillumination interferometer.

REFERENCES

1. "Diagnosis and management of dental caries throughout life," National Institutes of Health Consensus Statement 18 (NIH, 2001), pp. 1–30.
2. I. Pretty, "Caries detection and diagnosis: Novel technologies," J. Dent. **34**, 727–739 (2006).
3. D. Boston, "Incipient and hidden caries," Dent. Clin. North Am. **49**, xi–xii (2005).
4. J. Yang and V. Dutra, "Utility of radiology, laser fluorescence, and transillumination," Dent. Clin. North Am. **49**, 739–752 (2005).
5. A. Hall and J. Girkin, "A review of potential new diagnostic modalities for caries lesions," J. Dent. Res. **83**, C89–C94 (2004).
6. M. Huysmans, "Electrical measurements for early caries detection," in *Proceedings of the 4th Indiana Conference on Early Detection of Dental Caries*, G. Stookey, ed. (Indiana U. Press, 1999), pp. 123–142.
7. C. Longbottom and M. Huysmans, "Electrical measurements for use in caries clinical trials," J. Dent. Res. **83**, C76–C79 (2004).
8. S. White and D. Yoon, "Comparative performance of digital and conventional images for detecting proximal surface caries," Dentomaxillofac. Radiol. **26**, 32–38 (1997).
9. R. Ellwood, R. Davies, and H. Worthington, "Evaluation of a dental subtraction radiography system," J. Periodontal Res. **21**, 241–248 (1997).
10. F. Yanikoğlu and M. Analoui, "Ultrasonic methods for early caries detection," in *Proceedings of the 4th Indiana Conference on Early Detection of Dental Caries*, G. Stookey, ed. (Indiana U. Press, 1999), pp. 101–122.
11. F. Yanikoğlu, F. Öztürk, O. Hayran, M. Analoui, and G. Stookey, "Detection of natural white spot caries lesions by an ultrasonic system," Caries Res. **34**, 225–232 (2000).
12. B. Angmar-Mansson and J. ten Bosch, "Quantitative light-induced fluorescence (QLF): a method for assessment of incipient caries lesions," Dentomaxillofac. Radiol. **30**, 298–307 (2001).
13. M. van der Veen and E. de Josselin de Jong, "Application of quantitative light-induced fluorescence for assessing early caries lesions," in *Monographs in Oral Science: Assessment of Oral Health*, R. Faller, ed. (Karger, 2001), pp. 144–162.

14. B. Colston, U. Sathyam, L. DaSilva, M. Everett, P. Stroeve, and L. Otis, "Dental OCT," Opt. Express **3**, 230–238 (1998).
15. A. Baumgartner, S. Dichtl, C. Hitzenberger, H. Sattmann, B. Robl, A. Moritz, A. Fercher, and W. Sperr, "Polarization-sensitive optical coherence tomography of dental structures," Caries Res. **34**, 59–69 (2000).
16. R. Jones, G. Huynh, G. Jones, and D. Fried, "Near-infrared transillumination at 1310-nm for the imaging of early dental decay," Opt. Express **11**, 2259–2265 (2003).
17. C. Bühler, P. Ngaotheppitak, and D. Fried, "Imaging of occlusal dental caries (decay) with near-IR light at 1310-nm," Opt. Express **13**, 573–582 (2005).
18. C. Pine, "Fibre-optic transillumination (FOTI) in caries diagnosis," in *Proceedings of the 1st Indiana Conference on Early Detection of Dental Caries*, G. Stookey, ed. (Indiana U. Press, 1996), pp. 51–65.
19. G. Davies, H. Worthington, J. Clarkson, P. Thomas, and R. Davies, "The use of fibre-optic transillumination in general dental practice," Br. Dent. J. **191**, 145–147 (2001).
20. P. Vacas-Jacques, G. Paez, and M. Strojnik, "Pass-through photon-based biomedical transillumination," J. Biomed. Opt. **13**, 041307 (2008).
21. G. Paez, M. Strojnik, and M. Scholl, "Interferometric tissue characterization: I. Theory," Proc. SPIE **5883**, 58830Y (2005).
22. M. Strojnik and G. Paez, "Interferometric tissue characterization: II. Experimental," Proc. SPIE **5883**, 58830W (2005).
23. M. Strojnik and G. Paez, "Interferometric tissue characterization: III. Calibration," Proc. SPIE **5883**, 58830V (2005).
24. G. Paez, M. Strojnik, and S. Scholl, "Interferometric tissue characterization: IV. Material coherence function," Proc. SPIE **5883**, 58830X (2005).
25. P. Vacas-Jacques, M. Strojnik, and G. Paez, "Monte-Carlo simulation of photon transillumination time of flight," Proc. SPIE **6631**, 663114 (2007).
26. R. Jones and D. Fried, "Attenuation of 1310-nm and 1550-nm laser light through sound dental enamel," Proc. SPIE **4610**, 187–190 (2002).
27. D. Fried, J. Featherstone, C. Darling, R. Jones, P. Ngaotheppitak, and C. Bühler, "Early caries imaging and monitoring with near-infrared light," Dent. Clin. North Am. **49**, 771–793 (2005).
28. Y. Pan, R. Birngruber, J. Rosperich, and R. Engelhardt, "Low-coherence optical tomography in turbid tissue: theoretical analysis," Appl. Opt. **34**, 6564–6574 (1995).
29. L. Wang, S. Jacques, and L. Zheng, "MCML—Monte Carlo modeling of light transport in multi-layered tissues," Comput. Methods Programs Biomed. **47**, 131–146 (1995).
30. M. Yip and M. Carvalho, "A Monte-Carlo maplet for the study of the optical properties of biological tissues," Comput. Phys. Commun. **177**, 965–975 (2007).
31. S. Flock, B. Wilson, and M. Patterson, "Total attenuation coefficients and scattering phase functions of tissues and phantom materials at 633 nm," Med. Phys. **14**, 835–841 (1987).
32. W. Cheong, S. Prahl, and A. Welch, "A review of the optical properties of biological tissues," IEEE J. Quantum Electron. **26**, 2166–2185 (1990).
33. J. Ramella-Roman, S. Prahl, and S. Jacques, "Three Monte Carlo programs of polarized light transport into scattering media: part I," Opt. Express **13**, 4420–4438 (2005).
34. J. Ramella-Roman, S. Prahl, and S. Jacques, "Three Monte Carlo programs of polarized light transport into scattering media: part II," Opt. Express **13**, 10393–10405 (2005).
35. M. Xu, "Electric field Monte Carlo simulation of polarized light propagation in turbid media," Opt. Express **12**, 6530–6539 (2004).
36. G. Xiong, P. Xue, J. Wu, Q. Miao, R. Wang, and L. Ji, "Particle-fixed Monte Carlo model for optical coherence tomography," Opt. Express **13**, 2182–2195 (2005).
37. J. Zijp, J. ten Bosch, and R. Groenhuis, "HeNe-laser light scattering by human dental enamel," J. Dent. Res. **74**, 1891–1898 (1995).
38. D. Fried, R. Glena, J. Featherstone, and W. Seka, "The nature of light scattering in dental enamel and dentin at visible and near-IR wavelengths," Appl. Opt. **34**, 1278–1285 (1995).
39. B. Pogue and M. Patterson, "Review of tissue simulating phantoms for optical spectroscopy, imaging and dosimetry," J. Biomed. Opt. **11**, 041102 (2006).
40. H. van Staveren, C. Moes, J. van Marle, S. Prahl, and M. van Gemert, "Light scattering in Intralipid-10% in the wavelength range of 400–1100 nm," Appl. Opt. **30**, 4507–4514 (1991).
41. S. Flock, S. Jacques, B. Wilson, W. Star, and M. van Gemert, "Optical properties of Intralipid: a phantom medium for light propagation studies," Lasers Surg. Med. **12**, 510–519 (1992).
42. M. Modell, V. Ryabukho, D. Lyakin, V. Lychagov, E. Vitkin, I. Itzkan, and L. Perelman, "Autocorrelation low coherence interferometry," Opt. Commun. **281**, 1991–1996 (2008).
43. R Development Core Team, *R: A Language and Environment for Statistical Computing* (R Foundation for Statistical Computing, 2008).